Nanoscale

Accepted Manuscript

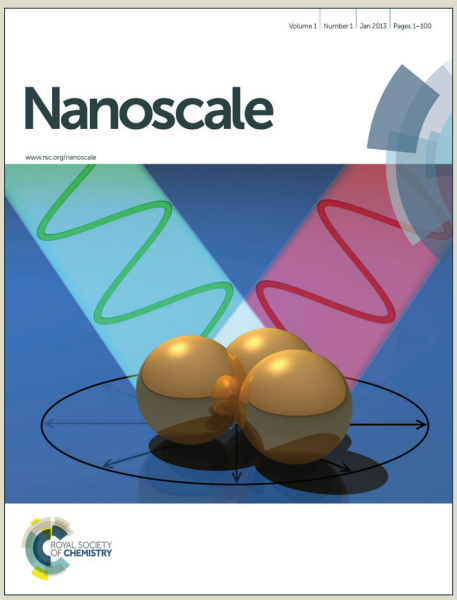

This is an *Accepted Manuscript*, which has been through the Royal Society of Chemistry peer review process and has been accepted for publication.

Accepted Manuscripts are published online shortly after acceptance, before technical editing, formatting and proof reading. Using this free service, authors can make their results available to the community, in citable form, before we publish the edited article. We will replace this *Accepted Manuscript* with the edited and formatted *Advance Article* as soon as it is available.

You can find more information about *Accepted Manuscripts* in the Information for Authors.

Please note that technical editing may introduce minor changes to the text and/or graphics, which may alter content. The journal's standard Terms & Conditions and the Ethical guidelines still apply. In no event shall the Royal Society of Chemistry be held responsible for any errors or omissions in this *Accepted Manuscript* or any consequences arising from the use of any information it contains.

ROYAL SOCIETY OF CHEMISTRY

www.rsc.org/nanoscale

Nanoscale

RSCPublishing

ARTICLE

The rational nanostructuring of surfaces for extraordinary icephobicity†

Cite this: DOI: 10.1039/x0xx00000x

Patric Eberle, Manish K. Tiwari*, Tanmoy Maitra and Dimos Poulikakos*

Received 00th January 2012,
Accepted 00th January 2012

DOI: 10.1039/x0xx00000x

www.rsc.org/

Icing of surfaces is commonplace in nature, technology and everyday life, bringing with it sometimes catastrophic consequences. A rational methodology for designing materials with extraordinary resistance to ice formation and adhesion remains however elusive. We show that ultrafine roughnesses can be fabricated, so that the ice nucleation-promoting effect of nanopits on surfaces is effectively counteracted by the presence of an interfacial quasiliquid layer. The ensuing interface confinement, strongly suppresses the stable formation of ice nuclei. We explain why such nanostructuring leads to the same extremely low, robust nucleation temperature of ~ −24 °C for over three orders of magnitude in RMS size (~0.1 to ~100 nm). Overlaying such roughnesses on pillar-microtextures harvests the additional benefit of liquid repellency and low ice adhesion. When tested at the temperature of −21 °C, such surfaces delayed the freezing of a sessile supercooled water droplet at the same temperature by a remarkable 25 hours.

Nanoscale Accepted Manuscript

Introduction

Ice formation is practically as old as the presence of water on earth and abundant in nature[1, 2] and technology.[3] Lack of adequate understanding of this process has led to humanity's vulnerability to serious accidents.[4] Therefore, a rational design of surfaces with exceptional ability to delay ice formation is of tremendous importance. A good starting point to this end is offered by recent advances in the understanding of surfaces which can repel liquid water effectively. It is widely recognized that roughness design is an integral part of generating highly liquid repellent surfaces[5, 6], which are termed superhydrophobic when the liquid is water.[7-9] Superhydrophobic surfaces, with micro- , nano-, or hierarchical roughnesses, have shown excellent repellency and low adhesion to water down to temperatures near and even lower than the freezing point.[5, 10-15] Additionally, roughness can critically affect the heterogeneous nucleation rate of ice at water/solid interfaces.[16, 17] Studies to date have reported both delays in ice formation on superhydrophobic surfaces[18-20] as well as the opposite effect; enhanced promotion of icing due to roughness.[16, 21, 22] Following a different approach compared to rough superhydrophobic surfaces, ultra smooth lubricant impregnated surfaces[23, 24] which exhibit remarkable droplet roll-off properties have been studied, also for anti-icing applications.[25, 26]

Clearly, a rational, approach to the design of surface texturing versus icing is needed to generate surfaces with extraordinary delay in ice formation.[17, 27] The anti-icing character of a surface can be quantified using two different metrics: the median nucleation temperature and the average ice nucleation delay time. The median nucleation temperature refers to the median temperature T_N at which ice nucleates in a sessile water droplet placed on a surface when the entire droplet/surface/surrounding gas system is cooled in a slow, quasi-steady manner. The average nucleation delay time refers to the average time τ_{av} required for ice to nucleate in a supercooled droplet[16] when the droplet is maintained at thermal equilibrium with its surroundings. Clearly both these metrics are obtained from a number of repeated measurements. Our measurements were performed at the condition of saturated humidity with respect to ice in order to avoid evaporation effects.[28]

Results and discussion

Thermodynamics shows that the free energy barrier ΔG for homogeneous ice nucleation in a supercooled liquid is higher than that for heterogeneous nucleation from contact with a solid surface.[17, 27] It is thus reasonable to assume that to delay icing in a supercooled droplet on a surface, the contact area A should be minimized and the ΔG for the formation of a stable ice embryo should be maximized. The ΔG can be altered through the parameters of ice-water contact angle Θ_{IW} and roughness radius of curvature R of the surface (see Equation S1 and S2, in Supplementary Information, section 1). The classic nucleation theory shows that at a given temperature, an ice nucleus must reach a critical size[17, 27] $r_c = 2\gamma_{IW}/\Delta G_{f,v}$ for freezing to start, where γ_{IW} and $\Delta G_{f,v}$ respectively, denote the ice-water interfacial energy and the volumetric free energy difference per unit volume between water and ice. At –25 °C, we obtain $r_c \approx$ 1.7 nm (Supplementary Information, section 1). The nucleation theory also shows that the roughness radius of curvature R has a strong bearing on ice nucleation when its value is near the critical nucleus radius r_c.

The r_c = 1.7 nm value provides us the first, order of magnitude estimate for tuning the surface roughness radius of curvature in order to suppress icing on the surface. We prepared to this end 11 different nanotextured surfaces with controlled roughness radii of curvature and wettability in order to develop a thermodynamic framework for surface nanostructuring leading to icing suppression. The nanotextured surfaces are labeled N1 to N8 (all hydrophobic) and N9 to N11 (all hydrophilic), respectively. After texturing, to render surfaces N1 to N8 hydrophobic, their surface energy was lowered by self-assembly of a perfluorodecyltrichlorosilane (FDTS) monolayer. The corresponding root mean square (RMS) roughness values are enumerated in Tables 1 and 2. For hierarchical morphology, an optimized nanotexture was then implemented on top of micropillar surfaces. Table 3 reports the geometric features of the Si micropillars and the symbols A1 through C2 denote the different micro-topographies tested.

Salient morphology examples are illustrated in Fig. 1a-d and Supplementary Information Fig. S2. The uniformity of surface topography in Fig. 1d (an atomic force microscope (AFM) scan on FDTS-coated smooth N1 substrate) confirms the uniformity of the monolayer coating.[29] The measured water droplet contact angles (CA) in advancing mode are shown in Fig. 1e and 1f. The corresponding receding angles are reported in Supplementary Information Fig. S3.

Table 1 Roughnesses of nanostructures N1 – N6

	N1	N2	N3	N4	N5	N6
RMS Roughness [nm]	0.17 ±0.04	1.25 ±0.2	1.6 ±0.1	2.3 ±0.2	6.2 ±0.9	14.6 ±3.0

Table 2 Roughnesses of nanostructures N7-Al-Ref

	N7	N8[a]	N9	N10	N11	Al-Ref
RMS Roughness [nm]	41.3	~173	0.17 ±0.04	20.8	41.3	150

[a] roughness estimated from SEM image

Table 3. Geometrical parameters of pillar surfaces.

	A1	A2	B1	B2	B3	C1	C2
Diameter [μm]	13	13	5	5	5	2.5	2.5
Pitch [μm]	23	33	9	13	18	4.5	6.5
Height [μm]	10	10	10	10	10	6	6
Φ Ratio	0.25	0.12	0.25	0.12	0.06	0.25	0.12

Nanoscale Accepted Manuscript

 This journal is © The Royal Society of Chemistry 2013

Nanoscale

RSCPublishing

ARTICLE

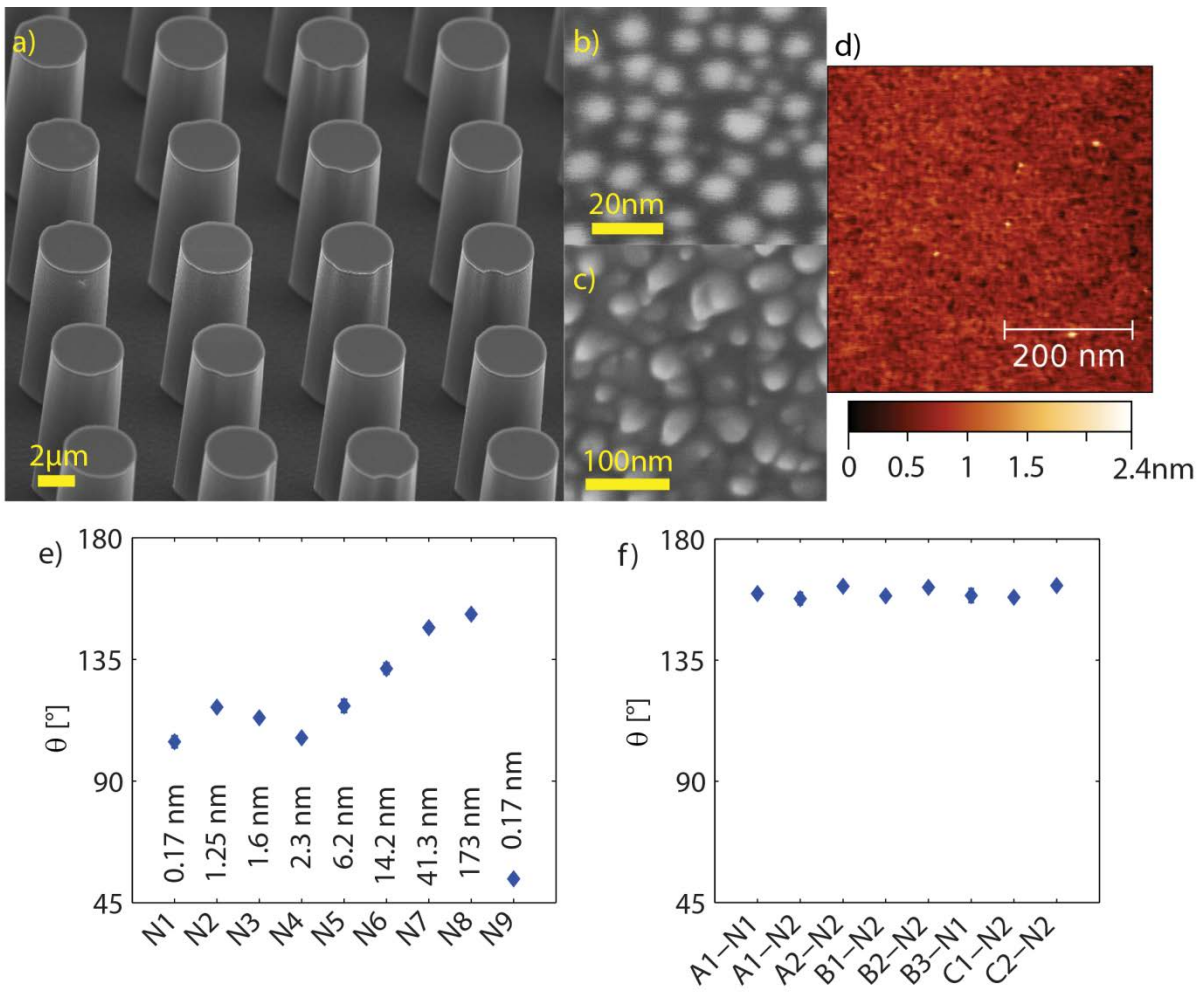

Fig. 1 a) SEM image of a micro-pillar structure with smooth sidewalls (type B1: diameter 5 µm, pitch 9 µm; image obtained with 45° tilted angle view). b) E-beam evaporated gold-dots with diameters of 10-15 nm formed on a SiO2 surface due to dewetting of the gold film. The dots were passivated with a thin SiO2 layer from top (nanostructure N2). c) Cryogenically etched SiO2 layer used as nanostructure N6. d) AFM scan of a FDTS coated polished Si surface. The ultralow surface roughness and minimal presence of bumps indicate a large and uniform monolayer FDTS coating. e) Water-air advancing contact angles of nanostructured SiO2 surfaces. The numeric values represent the RMS roughness. N10 and N11 were completely wetting and are, thus, not shown in figure. f) Water-air advancing contact angles of hierarchical micro-pillar substrates with SiO2 nanostructure N1 and N2 coated with FDTS.

The box plots in Fig. 2a show the measured nucleation temperatures on the nanotextured surfaces; each box summarizes 15-25 distinct measurements. In all our tests, the nucleation was detected by the onset of the recalescent stage of freezing. The Supplementary Information, section 9, details how we use high-speed video recording to detect this onset of freezing and, thus, the stable ice nucleation. A very important surprising finding of these experiments is that for the nanostructured substrates, T_N changes very little even with three orders of magnitude change in the RMS roughness (0.17 - 173 nm). The finding can be explained after a careful reconsideration and advancement of the nucleation theory (predictions shown in Fig. 2b). The ratio of free energy barriers for heterogeneous to homogeneous nucleation *f*, which is less

Nanoscale Accepted Manuscript

than unity (Supplementary Information, section 4), is a function of the roughness radius of curvature R , that is, not simply the RMS roughness. Fig. 2c and 2d show plots of f for convex (bumps) and concave (pits) roughness cases. The different curves in Fig. 2c and 2d correspond to different contact angles, which are intimately related to specific surface chemistry. It is clear that only when R is less than $10r_c$ does it affect the free energy barrier. Starting from a flat surface, with decrease in R the convex nanobumps on a surface should suppress nucleation while concave nanopits should promote it.[17, 27] Therefore, the discussion on the influence of the nanotexture should be primarily focused on the presence, distribution and interplay of necessarily coexisting nanobumps and nanopits.

Typically, a surface possesses a distribution of R values. The dashed blue curve in Fig. 2b plots the expected change in T_N as a function of R on surface with 15% of its area occupied by concave nanopits and for a constant typical Θ_{IW} = 100°. The nucleation theory, even when extended to account for melting point depression (the red curve) fails to predict the measured insensitivity of nucleation temperature with nanotexture. The reason for this can be understood by carefully analyzing the interfacial energy balance of an ice crystal nucleating in a nanopit, which is shown schematically in Fig. 2e and discussed in further details afterwards. Before getting into the physical explanation, we must analyze the exact morphological details of our nanotextures.

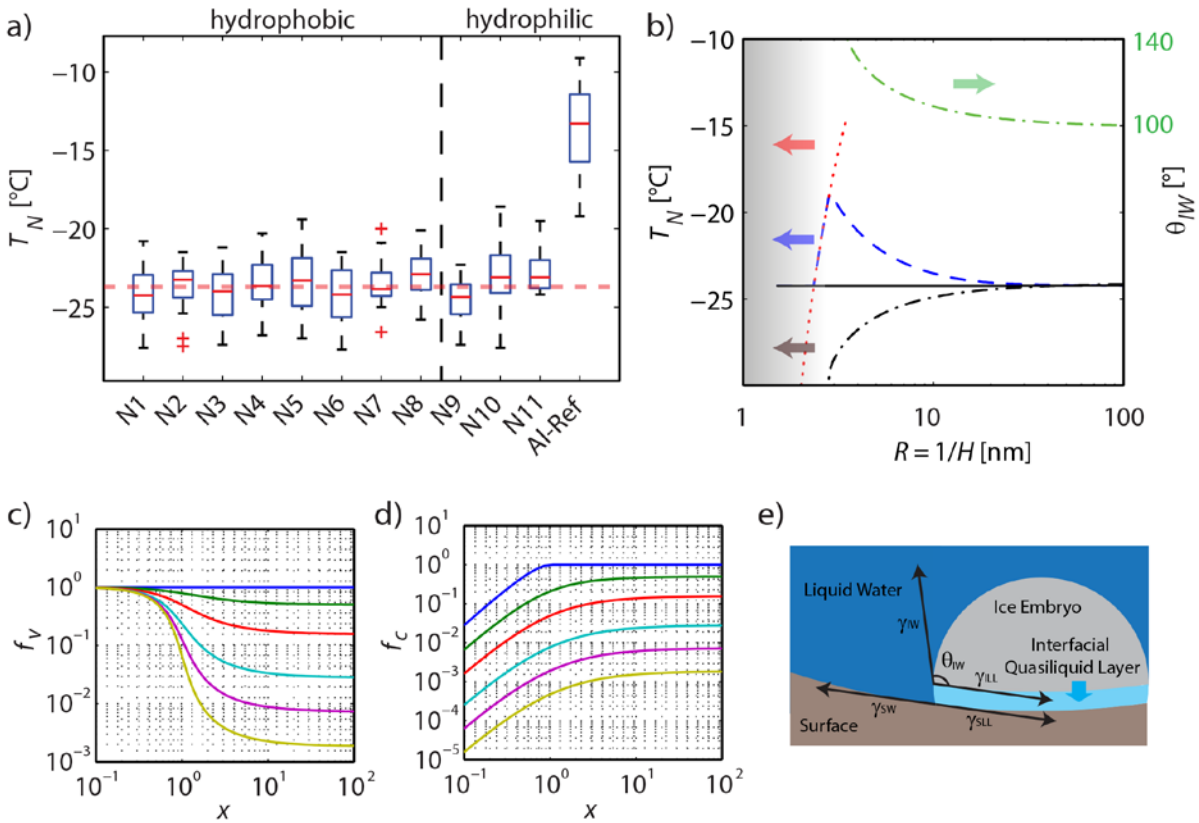

Fig. 2 a) Measured nucleation temperatures on nanostructured substrates N1-N11 and on a reference aluminum substrate. The red dashed line illustrates the nearly constant median T_N for different surface nanoscale roughnesses for hydrophobic N1-N8 and hydrophilic substrates N9-N11. The bottom and top line of the box represent the first and third quartile of the measured nucleation temperatures, and the red solid line inside the box shows the median. Lower and upper whiskers are connected with the box using black dashed lines. The outliers when present are shown as red crosses. b) T_N calculations from nucleation theory as a function of roughness curvature radius for a substrate with 15% of its area covered with concave nanoscale pits. The blue dashed line shows the results for constant Θ_{IW} = 100° and the black solid line for Θ_{IW} progressively increasing with decreasing roughness radius of curvature for the nanopits. The Θ_{IW} variation occurs due to the presence of a quasiliquid layer (see Supplementary Information, section 6). The red dotted line shows the depressed melting point in the nanoscale pits according the Gibbs-Thomson relation (see Supplementary Information, section 6) and the grey shaded area represents the range of roughness curvature radius where the melting point is depressed through confinement effects below the T_N of a flat substrate. The black dash-dotted line shows the T_N relation for a hypothetical surface with 100% of its area occupied by concave nanoscale pits and the coexisting bumps being perfectly sharp ($R=0$). The geometrical factor f plotted against the ratio $x=R/r_c$ for c) convex spherical surface roughness element (a bump) and d) concave spherical surface roughness element (a pit) according Equation S22 and S23 in the Supplementary Information, section 4. Different curves are obtained with $\cos(\Theta_{IW})$ = −1, 0, 0.5, 0.8, 0.9, 0.95 starting from the top, thereby spanning the Θ_{IW} range from 180° to 18.2°. e) Interface confinement on heterogeneously formed ice embryo with interfacial quasiliquid layer in a nanoscale cavity (nanopit).

Nanoscale Accepted Manuscript

 This journal is © The Royal Society of Chemistry 2013

Nanoscale

RSCPublishing

ARTICLE

In Fig. 3a and 3b we show two examples of the actual surface texture and roughness radii of curvature (superposed as a color plot on the topography image, generated using AFM scans) on the N6 and the N1 surfaces. The curvature radii values are markedly smaller for the rougher substrate N6 (RMS roughness of ~14.6 nm), compared to the ultra-smooth substrate N1 (RMS roughness of ~0.17 nm). The distribution of concave (pit) curvature radii sizes as a function of the surface area fraction they occupy is shown in Fig. 3c and 3d. The radii of the nanopits on N1 remain well above $10r_c$ (Fig. 3c). On N6, a substantial ~15% of the area is occupied by nanopits with radii below $10r_c$ (Fig. 3d). It is expected that the nanopits underneath the droplet will be wetted by liquid due to the moderate inclinations of the nanopit side walls and a reasonably low intrinsic CA in the nanopit. The latter should be same as the CA on a smooth surface having the same chemical composition and in our work can be approximated as ~105° i.e. the value measured on smooth substrate N1. Therefore, from heterogeneous nucleation theory we should expect T_N to be substantially different on these surfaces.

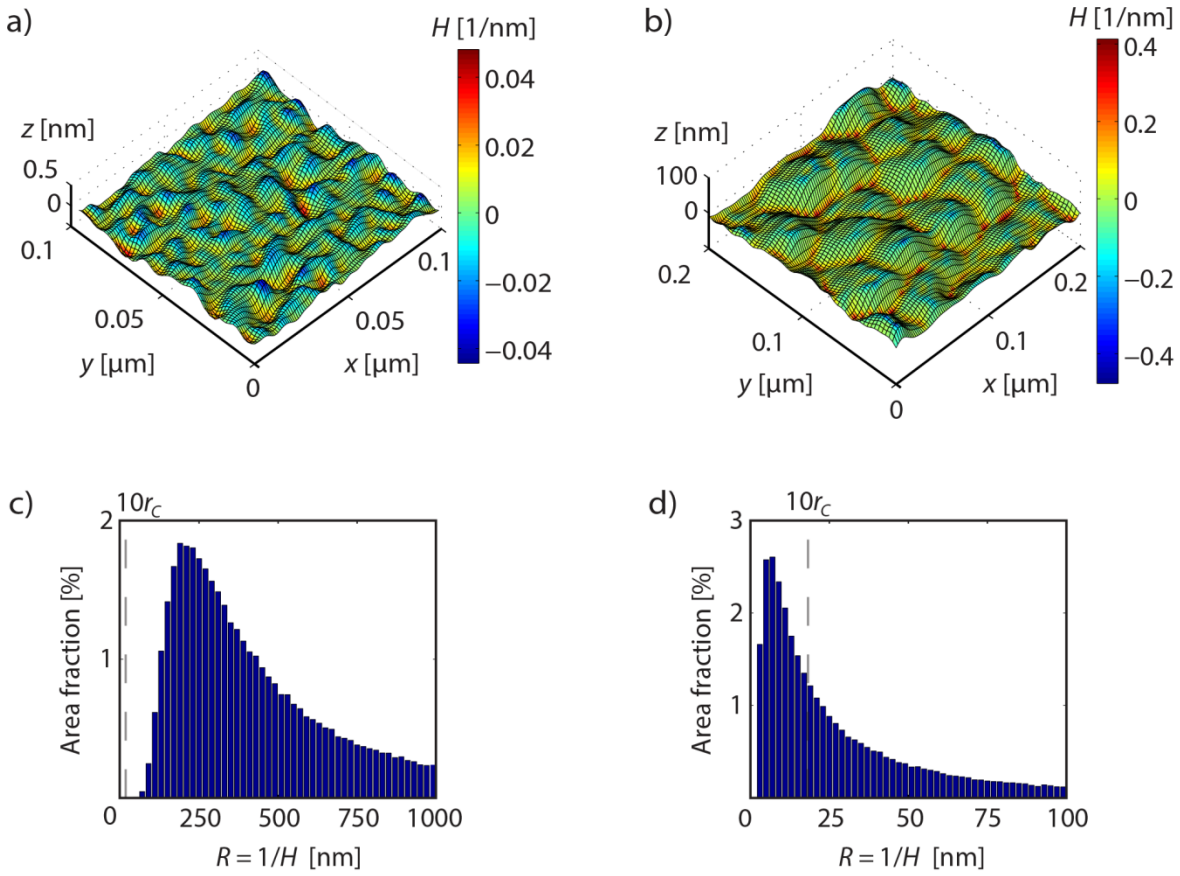

Fig. 3 Nanotexture of nanostructured surfaces a) N1 smooth (RMS roughness ~0.17nm) and b) rougher N6 (RMS roughness ~14.6nm), obtained by AFM scans with a super sharp tip (tip radius 2nm). The mean curvature H plotted through color intensities is overlaid on the height profile. The mean surface radius $R = 1/H$ and $H = \kappa_1 + \kappa_2$, where κ_1 and κ_2 represent the maximum and minimum curvature at a point. c) and d) show the area fraction occupied by nanopits plotted as a function of their roughness radius of curvature for substrates N1 and N6, respectively. While for N1, see a) and c), the pit curvature radii keep well above $10r_c$, for N6, see b) and d), the surface exhibits local regions with pit curvature radii smaller than $10r_c$. For N6, the area fraction of the regions with curvature radii smaller than $10r_c$ is ~15% (as determined from AFM scans). Substrates N1 and N6 exhibited the same median nucleation temperature.

Nanoscale Accepted Manuscript

Nanoscale RSCPublishing

ARTICLE

However, our measurement on these and a series of other nanostructured hydrophobic and hydrophilic substrates in a broad RMS roughness range going over three orders of magnitude (Fig. 2a) show very little change in T_N, despite the presence of nanopits as explained above. From the practical standpoint this is actually highly desirable: it allows the generation of a robust supericephobic morphology not requiring an ultra-precise tuning of the roughness. The physical explanation of the relative insensitivity of the measured T_N is provided in the following.

Crystallized water clusters, similar in size as ice nuclei, are known to possess a disordered amorphous layer at their surface.[30, 31] The disordering reaches a quasiliquid state at ice-vapor and ice-solid interfaces.[32] Careful experiments have established the presence of such quasiliquid layer for ice in contact with SiO_2[33] and surfaces treated with hydrophobic alkylsilanes.[34] Therefore, such a quasiliquid layer must also be present between the ice nucleus and our substrates. We show that presence of a quasiliquid layer on ice nuclei forming in nanoscale pits is profoundly important and we refer to it as a nanoscale interface confinement effect. In Fig. 2e we show that the presence of such quasiliquid like layer leads to a change of Θ_{IW} and fundamentally alters the nucleation characteristics.

A simple balance of the interfacial forces (see Fig. 2e and Supplementary Information, section 6) yields a modified Young's equation

$$\cos(\theta_{IW})\frac{\gamma_{IW}}{\beta}=\gamma_{SW}-\gamma_{SLL}-\frac{\gamma_{ILL}}{\beta}=\left(\gamma_{SW}+\frac{\gamma_{IW}}{\beta}-\gamma_{SI}\right)\mathrm{e}^{\frac{-d}{\xi}}-\frac{\gamma_{IW}}{\beta}, \quad (1)$$

where $\gamma_{ILL}, \gamma_{SLL}, \gamma_{SI}$ and γ_{SW} denote the surface energies of the interface between ice and quasiliquid layer, substrate and quasiliquid layer, substrate and ice, and substrate and liquid, respectively. $\beta=\left(\frac{R}{R-d}\right)^2$ and the symbols d and ξ represent the thickness of the quasiliquid layer and a characteristic decay length.[35] In Equation 1 the relations $\gamma_{ILL}=\gamma_{IW}\left(1-\mathrm{e}^{\frac{-d}{\xi}}\right)$ and $\gamma_{SLL}=\gamma_{SI}\,\mathrm{e}^{\frac{-d}{\xi}}+\gamma_{SW}\left(1-\mathrm{e}^{\frac{-d}{\xi}}\right)$ were used.[35]

For $R >> d$, Equation 1 can be rewritten (see Supplementary Information, section 6) as

$$\cos(\theta_{IW})\approx\left(\cos(\theta_{IW})^{*}+1\right)e^{\frac{-\left(d(R)-d^{*}\right)}{\xi}}-1\ , \quad (2)$$

where the superscript* denotes values on a flat substrate ($R = \infty$). Equation 1 and 2 are derived as Equation S24 and S26 in Supplementary Information, section 6. Equation 2 shows a dependence of Θ_{IW} with the radius of curvature R. The green dash-dotted line in Fig. 2b shows the variation of Θ_{IW} following Equation 2. If we account for this Θ_{IW} variation appearing due to the interface confinement effect, the T_N obtained from the corrected nucleation theory for surfaces with 15% area occupied by nanopits becomes constant, in agreement with our experiments. In other words, the Θ_{IW} variation counteracts the curvature dependent ice nucleation promotion in the nanoscale pits. Hence, the nucleation on "flat" regions (radii of curvature above$10r_c$) is dominant and results in the constancy of the T_N found in our experiments on nanostructured surfaces. In the limit of a hypothetical surface covered only with nanoscale pits (the bumps being assumed perfectly sharp, see schematic representation in Supplementary Information Fig. S4), the predicted T_N (see Fig. 2b) shows a strong decrease for $R < 10$ nm.

The effect of hierarchical morphology is shown in Fig. 4a. Hierarchical structures clearly exhibit a lower T_N than the corresponding substrates having only the nanostructure. This is due to a reduction in effective droplet surface contact area. The difference in T_N between a hierarchical and a simply nanostructured surface (Supplementary Information, section 1) can be expressed as

$$T_{N,H}-T_{N,N}\approx\frac{-1}{\lambda}ln\left(\frac{A_N}{A_H\Phi_{S,\mu}}\right)\ . \quad (3)$$

Here A denotes the droplet contact area, $\Phi_{S,\mu}$ denotes the fraction of the apparent droplet contact area touching the solid pillars[7] and λ is a substrate-specific constant (c.f. Equation 4 below), respectively. The symbols H and N in the subscripts denote hierarchical and nanostructures surface, respectively. The predictions from Equation 3 are plotted as stars in Fig. 4a, showing good agreement with experiments. The minor deviations can be explained by realizing that the nucleation rate is strong function of the density and the quality of nucleation sites[17] which could always vary ever so slightly in real roughness texturing (fabrication) processes. The Fig. 4a shows a ~2.5 °C reduction in T_N in going from nanostructured to hierarchical surfaces. This is equivalent to more than 2 orders

Nanoscale Accepted Manuscript

Nanoscale

RSCPublishing

ARTICLE

of magnitude difference in ice nucleation delay time, as we will show below.

Some salient average nucleation time τ_{av} measurements are plotted in Fig. 4b. To explain the trend of τ_{av} at temperatures away from the T_N, it is convenient to recast the heterogeneous nucleation rate as

$$J(T_N + \Delta T) = a\,exp(-\lambda \Delta T), \quad (4)$$

where a, λ denote constants and ΔT is the temperature change around T_N. Note that for each substrate shown in Fig. 4b, the T_N is different. The abscissa in the Fig. 4b is used to illustrate the change in the nucleation delay around the T_N for each substrate. Equation 4 is derived as Equation S9 in the Supplementary Information and can be used to predict $\tau_{av} = 1/J$ (see Supplementary Information, section 2). The prediction from Equation 4 is a straight line in logarithmic scale (Fig. 4b). For the measured τ_{av}, from Equation 4 we obtain $exp[-\lambda \cdot (1K)] \approx 10^{-1}$ for the A1-N1 surface. Similarly, for the hydrophilic substrate N9 we obtain $exp[-\lambda \cdot (1K)] \approx 10^{-2}$, corresponding to an order of magnitude steeper slope in Fig. 4b. The only difference between N1 and N9 nanostructures is the presence of FDTS monolayer on the former. Therefore, the difference in the two slopes in Fig. 4b can be attributed to the temperature dependence of Θ_{lw} due to the flexibility of the FDTS monolayer (discussed in detail in Supplementary Information, section 3). Additional experiments in Fig. 4b (red symbols) show that the hydrophobic nanotextured surface N1 and the hydrophobic hierarchical surface A1-N1 (both with FDTS monolayers), exhibit identical slopes underpinning the hypothesis that FDTS is responsible for a temperature dependent Θ_{lw}.

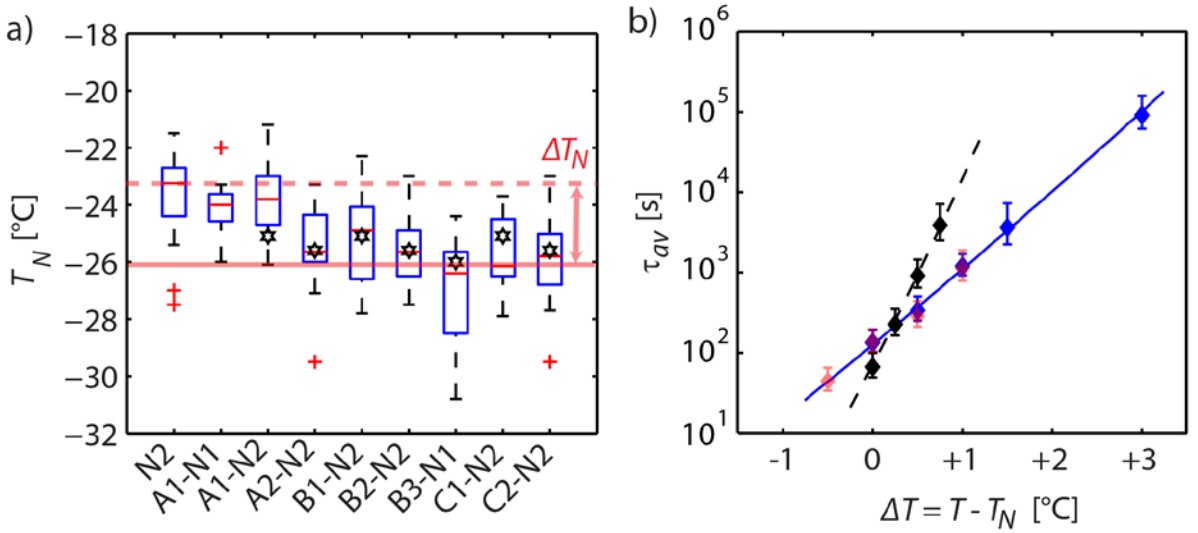

Fig. 4 a) Measured nucleation temperatures on substrates with hierarchical morphology. For the majority of substrates, the morphology consists of different micropillars with nanostructure N2 on top. The stars (∗) denote the predictions based on Equation 3. For comparison, hierarchical surfaces A1-N1 and B3-N1 (having the smoothest nanostructure) and substrate N2 (only nanostructured) are also included. The dashed and solid red line show a reduction of ~2.5 °C in median nucleation temperature (T_N) by overlaying nanostructure N2 on micropillars. This is equivalent to more than 2 orders of magnitude difference in the average ice nucleation delay time. b) Average ice nucleation delays (τ_{av}) of different substrates as a function of experimental temperature. To show the slope in ice nucleation delay around the median nucleation temperature (T_N) the delays are plotted as a function of temperature rise above the T_N for each substrate, $\Delta T = T - T_N$. The T_N values of the substrates (N1, A1-N1 and N9) were different (see Fig. 2a and 4b). The error bars show the statistical uncertainty from Poisson statistics for a confidence level of 95%. The blue diamonds correspond to the hierarchical hydrophobic substrate A1-N1, the red diamonds to the hydrophobic nanostructured surface N1 and the black ones to the hydrophilic substrate N9. The symbols represent the τ_{av}. For hydrophobic surfaces with FDTS layer, nucleation theory prediction (solid line), accounting for a linear decrease in Θ_{lw} with increasing temperature, shows excellent agreement with the measurements. Notwithstanding the greater slope for the hydrophilic surface, the low ice adhesion and dynamic droplet impact resistance make the hierarchical substrates preferable for icephobicity.

Nanoscale Accepted Manuscript

Nanoscale RSCPublishing

ARTICLE

The greater slope of icing delay time on the hydrophilic surface in Fig. 4b must be placed in proper perspective. Hydrophilic surfaces exhibit larger ice adhesion, which clearly correlates with the receding contact angle.[11] In fact, our estimates show nearly two orders of magnitude larger ice adhesion for the hydrophilic surfaces (such as N9) relative to the hierarchical hydrophobic A1-N1 surface. Furthermore, dynamic droplet impact resistance[13, 14] is another desired property of icephobic surfaces. In Supplementary Information Fig. S5 and Supplementary Movies S1 and S2, we clearly show that dynamically impacting water droplets, on substrates at −25 °C, adhere on the hydrophilic substrate N9 but bounce completely off on a typical hierarchical hydrophobic surface C1-N2. Finally, for surface A1-N1, a 1K rise in temperature decreases the nucleation rate by a factor of 10. The measured average ice nucleation delay times are shown as circles in Fig. 4b. The magnitude of the ice nucleation delay times experimentally demonstrated is indeed remarkable. The extreme ~25 hours delay at T_N + 3 °C (which comes to −21 °C for the A1-N1 surface) was obtained by measuring the nucleation rate and employing Poisson statistics (Supplementary Information, section 3 for details).[36] In all our experiments, including in the measurements at −21 °C, we only observed heterogeneous nucleation. This is expected[28] since our test condition was saturated with respect to ice (high humidity). In other studies in the literature, micro-nanostructured ZnO surfaces[20, 37] delayed the freezing of 10 µL droplets for ~3 hours at −10 °C. For polymer based superhydrophobic coatings on aluminium and silicon substrates delays of ~20 to 80 s (polymer) and ~1000 s (SiO_2), respectively, were measured at −20 °C for a droplet increasing in size over time.[16] The freezing delay of ~25 hours at −21 °C for our substrate is, to the best of our knowledge unprecedented, and justifies our reference to these surfaces as extraordinarily icephobic. For higher temperatures the freezing delays can be expected to increase even further.

Conclusions

We have presented here a rational approach, accounting for the intertwined effects of nucleation thermodynamics and superhydrophobicity, to develop surfaces with extreme anti-freezing properties. The approach to extraordinary resistance to ice formation boils down to designing superhydrophobic surfaces with low T_N through controlled nanostructuring guided by thermodynamic principles, and to employing such surfaces at temperatures slightly above the ice nucleation temperatures for which they are fabricated. The understanding and demonstrations provided in the current work should be of significant utility in dealing with ice surface interactions, in abundant occurrence in nature and technology.

Experimental

Surface preparation

Photolithography and cryogenic ICP etching were used to generate the micropillar structures. N1 is polished Si with inevitable native oxide (SiO_2) layer. Nanostructures N2, N4, N5, N6, N7, N10 and N11 were prepared by first depositing films of SiO_2 using PECVD, followed by etching in an ICP machine for different times. For N3, a gold nanodot (~15 nm diameter) structure was formed by dewetting of 1 nm thick gold on an SiO_2 film[38] followed by SiO_2 passivation. The nanostructure N8 was fabricated by glancing angle deposition of titanium using e-beam evaporation followed by SiO_2 passivation. To generate hierarchical morphologies, the required nanostructuring was applied after the micropillars were formed. For hydrophobic samples, an FDTS layer was applied by liquid phase self-assembly.

Surface characterization

AFM scans were performed in tapping mode using a super sharp, 2 nm silicon tip in an Asylum Research AFM. The contact angles were measured using an in house goniometer-type system. Further details on surface characterization are given in Supplementary Information, section 5.

Set-up and protocol

A double layer, transparent experimental chamber, fitted with several temperature and a humidity sensors, and controllably cooled using nitrogen vapor, was used. The chamber transparency facilitated droplet imaging with a high-speed camera (resolution ~0.05 mm). Using an ice bath, the inner the chamber was maintained at a saturated condition with respect to ice. High purity water (Type 1 Ultrapure Milli-Q, resistivity > 18 MΩcm) was used for the droplets in the freezing experiments.

We used two kinds of tests: nucleation temperature determination and ice nucleation delay measurement. In each case, freezing of the supercooled water droplet occurred in two distinct steps.[16] First a rapid recalescent stage (lasting ~ 10 ms) led to partial solidification of the droplet and turned it into a liquid solid mixture. This stage could be easily detected using our high speed video recording at 1000 frames per second, thus

Nanoscale Accepted Manuscript

Nanoscale

RSCPublishing

ARTICLE

yielding a time resolution of 1 ms. The Movie S3 shows the first stage freezing on surface N1. The onset of freezing is marked by a clear change in droplet image intensity and thus easily detectable. Following the recalescent step, the drops froze completely through a second, slower and isothermal stage lasting ~ 10's of seconds. Movies S4 and S5 show this step on the surface N1 and A2-N2, respectively.

For the nucleation temperature measurements, the chamber temperature was lowered at –0.31 K/min starting from an equilibrium condition at –14 °C. The error due to changes in the cooling rate is minimal (Supplementary Information, section 7).

For nucleation delay measurements, the temperature was held constant and the time of droplet nucleation was recorded. After the recalescent step, the second step followed inevitably. Since we detected the first step with ms precision, the accuracy of our reported nucleation delay is very high.

Further information about surface fabrication and experimental details are given in Supplementary Information, section 9.

Acknowledgements

The partial support for this work from the Swiss National Science Foundation (SNF) grant 200021_135479 is gratefully acknowledged.

Notes and References

Laboratory of Thermodynamics in Emerging Technologies, Mechanical and Process Engineering Department, ETH Zurich, 8092 Zurich, Switzerland

† Electronic Supplementary Information (ESI) available: thermodynamic framework and statistical methods for data analyses; details of ice nucleation delay measurements and prediction of the delays around the median nucleation temperature; additional SEM and AFM images not shown in the main paper and complete contact angle characterization; derivation of the nanoscale interface confinement effect; an error assessment, detailed results of droplet impact experiments on hydrophilic and hydrophobic substrates; methods for surface preparation and characterization; description of the experimental set up and protocols; five videos supporting the text. See DOI: 10.1039/b000000x/

1. Y. C. Liou, A. Tocilj, P. L. Davies and Z. C. Jia, *Nature*, 2000, **406**, 322-324.
2. Z. C. Jia, C. I. DeLuca, H. M. Chao and P. L. Davies, *Nature*, 1996, **384**, 285-288.
3. N. Dalili, A. Edrisy and R. Carriveau, *Renewable & Sustainable Energy Reviews*, 2009, **13**, 428-438.
4. R. W. Gent, N. P. Dart and J. T. Cansdale, *Philos T Roy Soc A*, 2000, **358**, 2873-2911.
5. X. Deng, L. Mammen, H. J. Butt and D. Vollmer, *Science*, 2012, **335**, 67-70.
6. A. Tuteja, W. Choi, M. L. Ma, J. M. Mabry, S. A. Mazzella, G. C. Rutledge, G. H. McKinley and R. E. Cohen, *Science*, 2007, **318**, 1618-1622.
7. A. Lafuma and D. Quere, *Nat Mater*, 2003, **2**, 457-460.
8. A. T. Paxson and K. K. Varanasi, *Nat Commun*, 2013, **4**, 1492.
9. G. Azimi, R. Dhiman, H. M. Kwon, A. T. Paxson and K. K. Varanasi, *Nat Mater*, 2013, **12**, 315-320.
10. A. J. Meuler, G. H. McKinley and R. E. Cohen, *ACS Nano*, 2010, **4**, 7048-7052.
11. A. J. Meuler, J. D. Smith, K. K. Varanasi, J. M. Mabry, G. H. McKiney and R. E. Cohen, *ACS Appl Mater Inter*, 2010, **2**, 3100-3110.
12. A. Alizadeh, M. Yamada, R. Li, W. Shang, S. Otta, S. Zhong, L. H. Ge, A. Dhinojwala, K. R. Conway, V. Bahadur, A. J. Vinciquerra, B. Stephens and M. L. Blohm, *Langmuir*, 2012, **28**, 3180-3186.
13. A. Alizadeh, V. Bahadur, S. Zhong, W. Shang, R. Li, J. Ruud, M. Yamada, L. H. Ge, A. Dhinojwala and M. Sohal, *Appl Phys Lett*, 2012, **100**.
14. T. Maitra, M. K. Tiwari, C. Antonini, P. Schoch, S. Jung, P. Eberle and D. Poulikakos, *Nano Lett*, 2014, **14**, 172-182.
15. C. Antonini, M. Innocenti, T. Horn, M. Marengo and A. Amirfazli, *Cold Reg Sci Technol*, 2011, **67**, 58-67.
16. S. Jung, M. Dorrestijn, D. Raps, A. Das, C. M. Megaridis and D. Poulikakos, *Langmuir*, 2011, **27**, 3059-3066.
17. H. R. Pruppacher and J. D. Klett, *Microphysics of Clouds and Precipitation*, Kluwer Academic Publishers, New York, Boston, Dordrecht, London, Moscow, 1997.
18. P. Tourkine, M. Le Merrer and D. Quere, *Langmuir*, 2009, **25**, 7214-7216.
19. M. He, J. J. Wang, H. L. Li and Y. L. Song, *Soft Matter*, 2011, **7**, 3993-4000.
20. P. Guo, Y. M. Zheng, M. X. Wen, C. Song, Y. C. Lin and L. Jiang, *Adv Mater*, 2012, **24**, 2642-2648.
21. L. L. Cao, A. K. Jones, V. K. Sikka, J. Z. Wu and D. Gao, *Langmuir*, 2009, **25**, 12444-12448.
22. K. K. Varanasi, T. Deng, J. D. Smith, M. Hsu and N. Bhate, *Appl Phys Lett*, 2010, **97**.
23. T. S. Wong, S. H. Kang, S. K. Y. Tang, E. J. Smythe, B. D. Hatton, A. Grinthal and J. Aizenberg, *Nature*, 2011, **477**, 443-447.
24. J. D. Smith, R. Dhiman, S. Anand, E. Reza-Garduno, R. E. Cohen, G. H. McKinley and K. K. Varanasi, *Soft Matter*, 2013, **9**, 1772-1780.
25. K. Rykaczewski, S. Anand, S. B. Subramanyam and K. K. Varanasi, *Langmuir*, 2013, **29**, 5230-5238.
26. P. Kim, T. S. Wong, J. Alvarenga, M. J. Kreder, W. E. Adorno-Martinez and J. Aizenberg, *ACS Nano*, 2012, **6**, 6569-6577.
27. N. H. Fletcher, *J Chem Phys*, 1958, **29**, 572-576.
28. S. Jung, M. K. Tiwari, N. V. Doan and D. Poulikakos, *Nat Commun*, 2012, **3**.
29. M. J. Pellerite, E. J. Wood and V. W. Jones, *J Phys Chem B*, 2002, **106**, 4746-4754.
30. C. C. Pradzynski, R. M. Forck, T. Zeuch, P. Slavicek and U. Buck, *Science*, 2012, **337**, 1529-1532.
31. V. Buch, S. Bauerecker, J. P. Devlin, U. Buck and J. K. Kazimirski, *Int Rev Phys Chem*, 2004, **23**, 375-433.
32. G. Malenkov, *J Phys-Condens Mat*, 2009, **21**.

Nanoscale Accepted Manuscript

33. S. Engemann, H. Reichert, H. Dosch, J. Bilgram, V. Honkimaki and A. Snigirev, *Phys Rev Lett*, 2004, **92**.
34. M. Mezger, S. Schoder, H. Reichert, H. Schroder, J. Okasinski, V. Honkimaki, J. Ralston, J. Bilgram, R. Roth and H. Dosch, *J Chem Phys*, 2008, **128**.
35. R. R. Vanfleet and J. M. Mochel, *Surf Sci*, 1995, **341**, 40-50.
36. B. Zobrist, T. Koop, B. P. Luo, C. Marcolli and T. Peter, *J Phys Chem C*, 2007, **111**, 2149-2155.
37. P. Guo, M. Wen, L. Wang and Y. Zheng, *Nanoscale*, 2013, DOI: 10.1039/c3nr04061e.
38. J. Albuschies, M. Baus, O. Winkler, B. Hadam, B. Spangenberg and H. Kurz, *Microelectron Eng*, 2006, **83**, 1530-1533.

Nanoscale Accepted Manuscript

 This journal is © The Royal Society of Chemistry 2013